



Macroscopic, theoretical simulation and spectroscopic investigation on the immobilization mechanisms of Ni(II) at cryptomelane/water interfaces

Chunfang Wu ^a, Lei Chen ^a, Shitong Yang ^{b,a,*}, Yawen Cai ^a, Lin Xu ^a, Xilin Wu ^c, Haibo Qin ^d, Zhiyong Liu ^a, Lanhua Chen ^a, Shuaow Wang ^{a,**}

^a State Key Laboratory of Radiation Medicine and Protection, School for Radiological and Interdisciplinary Sciences (RAD-X) and Collaborative Innovation Center of Radiation Medicine of Jiangsu Higher Education Institutions, Soochow University, Suzhou, 215123, PR China

^b Department of Earth and Planetary Science, Graduate School of Science, The University of Tokyo, 7-3-1 Hongo, Bunkyo-ku, Tokyo, 113-0033, Japan

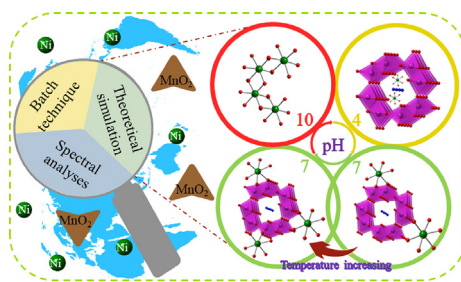
^c College of Geography and Environmental Science, Zhejiang Normal University, Jinhua, 321004, PR China

^d State Key Laboratory of Environmental Geochemistry, Institute of Geochemistry, Chinese Academy of Sciences, Guiyang, 550081, PR China

HIGHLIGHTS

- Interaction mechanisms of Ni(II) with cryptomelane were explored by combining multiple techniques.
- Relative contributions of different uptake processes were verified from ligand extraction data.
- Ni(II) binding modes were clearly identified with theoretical simulation and spectroscopic analyses.
- Temperature rising enhanced the sorption amount of Ni(II) in double corner-shared binding mode.
- Research findings facilitated the assessment of Ni(II) migration and fate in Mn-riched environment.

GRAPHICAL ABSTRACT



ARTICLE INFO

Article history:

Received 12 June 2018

Received in revised form

4 July 2018

Accepted 6 July 2018

Available online 7 July 2018

Handling Editor: Y Yeomin Yoon

Keywords:

Ni(II)

Cryptomelane

ABSTRACT

In the present study, the macroscopic sorption behaviors and microscopic immobilization mechanisms of Ni(II) at cryptomelane/water interfaces were explored using the combination of batch sorption technique, desorption procedure, theoretical simulation, X-ray diffraction (XRD), Fourier transform infrared spectroscopy (FTIR), X-ray photoelectron spectroscopy (XPS) and extended X-ray absorption fine structure (EXAFS) analyses. The good simulation of the pseudo-second-order model on the sorption kinetics data suggests a driving force of chemical sorption rather than mass transport or physical interaction. The sorption trends and uptake mechanisms are obviously related to the solution pH, with cation exchange or outer-sphere surface complexation at an acidic pH of 4.0, inner-sphere surface complexation in both the edge-shared (ES) and double corner-shared (DCS) modes at a neutral pH of 7.0, and precipitation of α -Ni(OH)₂(s) phase at a highly alkaline pH of 10.0. The gradual increase of Ni(II) sorption amount with solution temperature rising from 293 K to 333 K is consistent with the increased ratio of the weak DCS

* Corresponding author. Department of Earth and Planetary Science, Graduate School of Science, The University of Tokyo, 7-3-1 Hongo, Bunkyo-ku, Tokyo, 113-0033, Japan.

** Corresponding author.

E-mail addresses: shitongyang-dmn@outlook.com (S. Yang), shuaowang@suda.edu.cn (S. Wang).

Theoretical simulation
Spectroscopic analyses
Immobilization mechanisms

configuration. The research findings herein can help us better understand the migration and transformation trends of Ni(II) in the manganese mineral-riched aquatic environment.

© 2018 Elsevier Ltd. All rights reserved.

1. Introduction

Heavy metal pollution has gained wide concern from the public and environmentalists. Nickel(II) is widely present in the wastewaters discharged from various industrial processes such as pesticides, electrolysis, metallurgy, dyes and etc. Numerous studies have proved the toxicities of Ni(II) to the hydrophytes, aquatic animals and human beings (Cempel and Nikel, 2006; Wang et al., 2016). Thereby, it is essential to explore the speciation and migration trends of Ni(II) in the geological environment.

Natural minerals significantly affect the physicochemical behaviors of contaminants in the aquatic systems. Multiple experimental, modelling and spectral approaches have been applied to infer the potential sorption mechanisms of Ni(II) on a series of minerals. Specifically, the retention of Ni(II) by the clay minerals with exchangeable ions in the interlayer is attributed to outer-sphere surface complexation and/or cation exchange at acidic pH, inner-sphere surface complexation and/or (co)precipitation at neutral and alkaline pH (Dähn et al., 2002; Ren et al., 2013; Sheng et al., 2011a, b; Siebecker et al., 2014; Yang et al., 2015; Zhao et al., 2017). By contrast, the immobilization of Ni(II) by the Al/Si/Fe/Mn (hydro)oxides without the interlayer structure is controlled by inner-sphere surface complexation (Grangeon et al., 2017; Lefkowitz and Elzinga, 2017; Sheng et al., 2011a, b; Xu et al., 2007), lattice substitution (Manceau et al., 2007; Peacock and Sherman, 2007; Peacock, 2009; Peña et al., 2010; Singh et al., 2002) and/or Ni-Al/Si (co)precipitation (Scheckel and Sparks, 2000; Tan et al., 2014). The differences between the foregoing Ni(II)-clays and Ni(II)-metal (hydro)oxides systems may be due to the different types, structures and properties of the used minerals as well as the disparate environmental conditions of the sorption experiments. In view of this, further work is still needed to definitely verify the interactions of Ni(II) with more kinds of minerals.

Cryptomelane, as a manganese oxide mineral, is widespread in the natural soil and aquatic systems. Previous researchers have conducted several studies to explore the sorption performance and immobilization mechanisms of cryptomelane for various toxic heavy metal ions, e.g., Cs(I), Zn(II), Pb(II), Co(II), Cd(II), Cr(III), U(VI) and Th(IV) (El-Naggar et al., 1993; Ghoneimy, 1997; Ghaly et al., 2018; Li et al., 2015; Lu et al., 2007; Randall et al., 1998). To the best of our knowledge, no data are available to clearly elaborate the interaction mechanisms of Ni(II) with cryptomelane. In the present work, batch sorption experiments were performed to explore the influence of multiple environmental factors on the macroscopic sorption trends of Ni(II) on cryptomelane. In addition, the microscopic immobilization mechanisms of Ni(II) were identified by combining desorption procedure, theoretical simulation and spectral approaches (i.e., FTIR, XPS and EXAFS).

2. Materials and methods

2.1. Chemical reagents

Nickel nitrate hexahydrate ($\text{Ni}(\text{NO}_3)_2 \cdot 6\text{H}_2\text{O}$) with analytical purity were purchased from Sigma-Aldrich Trading Co., Ltd (Shanghai, China). The rest of chemical reagents were obtained from Sinopharm Chemical Reagent Co., Ltd. All the solutions were

prepared by using the Milli-Q water.

2.2. Preparation and characterization of cryptomelane

The cryptomelane mineral was synthesized by adopting the method as described in the literature (Calvert et al., 2008; Huang et al., 2010; Sithambaram et al., 2009; Wang and Li, 2002). The XRD pattern of the synthesized sample was recorded by using a Bruker D8 Advance diffractometer with the radiation of $\text{Cu K}\alpha$ ($\lambda = 0.15406 \text{ nm}$). The FTIR spectrum within the wavenumber of $4000\text{--}400 \text{ cm}^{-1}$ was collected on a Thermo Nicolet 6700 spectrometer. The surface charges of cryptomelane in the pH range of 2.0–10.0 were determined by using a Zetasizer Nano ZS90 Analyzer. The TG curve within $70\text{--}900^\circ\text{C}$ was measured with the aid of NETZSCHSTA 449F3 instrument under a N_2 flow.

2.3. Macroscopic sorption experiments

The sorption experiments of Ni(II) on cryptomelane were performed in a series of 10 mL centrifuge tubes as a function of different environmental factors. In brief, the pH values of the suspensions containing cryptomelane, NaNO_3 and Ni(II) were adjusted with trace amounts of HNO_3/NaOH solutions. The increase for the total volumes of the uptake systems was negligible and thus the deviation for the solid/liquid ratio was less than 1%. After oscillating the centrifuge tubes for a certain time, the solid and liquid phases were separated by centrifugation. The supernatants were filtrated by using $0.22 \mu\text{m}$ filter membrane followed by the measurement of Ni(II) concentration (C_e , mmol/L) with inductively coupled plasma-atomic emission spectrometry. The sorption percent ($S\% = (C_0 - C_e)/C_0 \cdot 100\%$) and amount ($q_e = (C_0 - C_e) \cdot V/m$, mmol/g) were calculated from the initial (C_0 , mmol/L) and final concentration (C_e) of Ni(II) as well as the solid dosage (m/V, g/L) of the uptake system.

2.4. Desorption experiments

To help determine the specific driving forces that contribute to the sequestration of Ni(II) by cryptomelane, additional extraction experiments were carried out by using $\text{CH}_3\text{COONH}_4$ (possessing excellent ion-exchange capacity for heavy metal ions) and EDTA-2Na (showing strong chelating property for heavy metal ions) as the eluents (Gao et al., 2003; Salinas et al., 2000; Xu et al., 2016). Specifically, the Ni(II)-loaded cryptomelane samples were sequentially soaked into 10.0 mM of $\text{CH}_3\text{COONH}_4$ solution and 2.0 mM of EDTA-2Na solution. The subsequent experimental procedures were similar to those described in section 2.3. The fraction desorbed by $\text{CH}_3\text{COONH}_4$ represents the uptake mechanism of cation exchange and/or outer-sphere surface complexation, while that extracted by EDTA-2Na represents the retention mechanism of inner-sphere complexation. The fraction remaining after EDTA-2Na extraction represents the precipitation mechanism.

2.5. Spectral data collection and analysis

XPS spectra of the Ni(II)-loaded cryptomelane samples were recorded on Kratos Axis Ultra DLD spectrometer (SHIMADZU, Japan) with the X-ray energy of $\text{Al K}\alpha$ (1486 eV). Ni K-edge EXAFS

spectra were obtained at BL14W1 of Shanghai Synchrotron Radiation Facility (SSRF, China). EXAFS data analyses were performed by Athena and Artemis software (Ankudinov and Rehr, 1997; Ravel and Newville, 2005). Based on the crystal structures of $\text{Ni}(\text{NO}_3)_2 \cdot 6\text{H}_2\text{O}$, $\text{Ni}(\text{OH})_2(s)$ and $\text{Ca}_3\text{Ni}_{0.92}\text{Mn}_{1.08}\text{O}_6$ (Vicat et al., 1986), the theoretical scattering phases and amplitudes of Ni–O, Ni–Mn and Ni–Ni backscattering paths were calculated by using FEFF7.

3. Results and discussion

3.1. Characterization

Fig. 1A shows the XRD pattern of the synthesized solid powder. The diffraction peaks at $\sim 12.8^\circ$, $\sim 18.0^\circ$, $\sim 25.8^\circ$ and $\sim 28.8^\circ$ are consistent with the crystallographic information of cryptomelane phase (Calvert et al., 2008). For the FTIR spectrum (**Fig. 1B**), the wide band at 3450 cm^{-1} is assigned to the stretching vibration of O–H bond or H_2O molecules. The peaks at 1635 and 1387 cm^{-1} are attributed to the strong bending vibration of O–H bond that combined with Mn atoms. The peaks within 1000 – 400 cm^{-1} represent the characteristic vibrations of Mn–O bonds (Deguzman et al., 1994; Gao et al., 2008; Kazazi, 2018; Sheng et al., 2010). The strong bands at 460 and 510 cm^{-1} can be attributed to the characteristic vibrations of the MnO_6 skeletal in a typical cryptomelane structure. The peak at 720 cm^{-1} is due to the stretching vibration of MnO_6 octahedra along the double-chain (Julien et al., 2004; Tizfahm et al., 2016). As shown in **Fig. 1C**, the surface potential of cryptomelane gradually decreases with the increase of solution pH and the zero point charge (pH_{Zpc}) value is defined to be ~ 4.6 . The TG curve (**Fig. 1D**) reveals the stepwise weight loss of cryptomelane with the change of temperature. Specifically, the slight decline of weight ($\sim 2.5\%$) within 70 – 255°C is due to the evaporation of

surface-related water. During the subsequent heating-up stage from 225 to 770°C , the cryptomelane weight gradually decreases from 97.5% to 90.1% . This phenomenon can be attributed to the loss of chemically adsorbed water and the structural oxygen from the framework (Chen et al., 2002; Villegas et al., 2005). No further weight loss can be observed as the calcination temperature higher than 770°C . Overall, the TG curve indicates that the cryptomelane mineral is rather stable over a wide temperature region.

3.2. Macroscopic sorption data

3.2.1. Sorption kinetics

Fig. S1 shows the time-dependent sorption data of Ni(II) on cryptomelane at 293 K and $\text{pH } 7.0$. Clearly, $\sim 48\%$ of the initial Ni(II) is retained during a relatively short time period of 0.5 h . Then, the sorption percentage increases rapidly to $\sim 70\%$ after 6 h and keeps almost unchanged with prolonged aging time. Similar variation trend is also observed for the sorption amount. In consideration of these phenomena, a contact time of 24 h was selected in the subsequent experiments to insure adsorption equilibrium. According to the simulation results of the pseudo-first-order and pseudo-second-order equations (see **Fig. S1** and **Table S1** in the Supporting Information (denoted as SI in the following text)) (Ho and McKay, 1999a, 1999b; Ho and Ofomaja, 2006; Ivanets et al., 2017), one can deduce that the immobilization of Ni(II) by cryptomelane at 7.0 is controlled by chemisorption rather than mass transport or physical interaction.

3.2.2. Effects of pH and ionic strength

The pH-dependent sorption trends of Ni(II) on cryptomelane is illustrated in **Fig. 2**. Specifically, the sorption percent of Ni(II) in 0.01 mol/L of NaNO_3 solution keeps almost constant at $\sim 30\%$ within

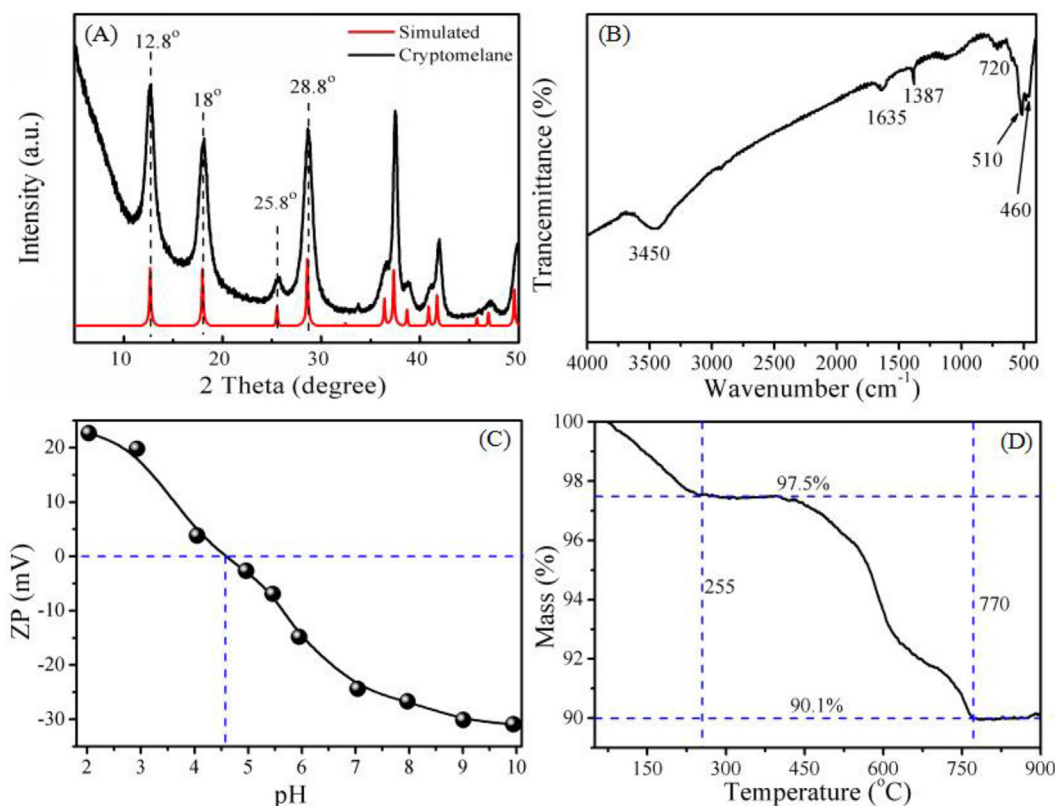


Fig. 1. XRD (A), FTIR (B), zeta potential (C) and TG curve (D) of cryptomelane.

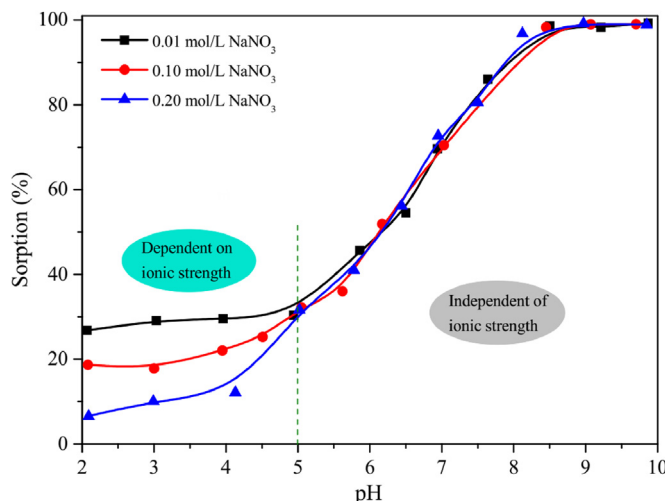


Fig. 2. Effect of pH and ionic strength on the sorption of Ni(II) on the cryptomelane. $T = 293\text{ K}$, $m/V = 0.5\text{ g/L}$, $C_{\text{Ni(II)}\text{initial}} = 1.0 \times 10^{-4}\text{ mol/L}$.

pH 2.0–5.0, then rises rapidly to ~100% as the pH value increases to 8.5, and remains at ~100% above the pH value of 8.5. The appearance of three sorption regions suggests the potential occurrence of different immobilization mechanisms, depending on the surface properties of cryptomelane and the speciation of Ni(II). Herein, the cryptomelane mineral exhibits a zero point charge (pH_{Zpc}) value of ~4.6 (Fig. 1C). According to the thermodynamic calculation predicted by Visual MINTEQ ver. 3.1 (Gustafsson, 2018), Ni^{2+} is the main species of Ni(II) over a wide pH range of 2.0–8.5 (Fig. S2). Obviously, the Ni^{2+} ions are hardly adsorbed by cryptomelane at pH 2.0–5.0 due to electrostatic repulsion. While at $\text{pH} > 5.0$, Ni(II) can be readily immobilized by the deprotonated surface sites of cryptomelane. One can see from Fig. S2 that the $\text{Ni(OH)}_2(s)$ precipitation occurs from an alkaline pH value of 8.7. Therefore, the rapid rising of Ni(II) uptake percentage in the pH range of 5.0–8.5 is not due to precipitation. Beyond all doubt, the precipitation mechanism will significantly promote the efficient immobilization of Ni(II) at $\text{pH} > 8.7$.

As shown in Fig. 2, the increase of ionic strength inhibits the retention of Ni(II) at $\text{pH} < 5.0$. Herein, the increased electrolyte concentration can result in the coagulation of cryptomelane particles, the expansion of the thickness of electrical diffused double layer and the decrease of Ni(II) ion activity in solution. These factors synergistically suppress the attachment of Ni(II) onto cryptomelane (Hu et al., 2010; Mercer and Tobiason, 2008). Nevertheless, the apparent dependence of sorption trends on ionic strength suggests that cation exchange (with the H^+ or K^+ ions in the channels) and/or outer-surface complexation (via electrostatic interaction) are the main immobilization mechanisms of Ni(II) by cryptomelane below pH 5.0. From Fig. 2, no apparent influence of ionic strength variation on Ni(II) immobilization can be observed at pH value above 5.0. By considering the previous theories on ionic strength-related sorption trends and the speciation diagram of Ni(II) (Fig. S2) (Bui and Choi, 2010; Yang et al., 2011, 2012; Yuan et al., 2017), one can make a conclusion that inner-sphere complexation is the predominant retention mechanism at $5.0 < \text{pH} < 8.7$ and the occurrence of precipitation dominates at pH value higher than 8.7.

3.2.3. Sorption isotherms

Fig. 3 displays the equilibrium sorption data of Ni(II) on cryptomelane at 293, 313 and 333 K. Clearly, the sorption amount rises with the increase of equilibrium Ni(II) concentration (C_e , mmol/L) and a sorption plateau appears at higher C_e value. The classical L-

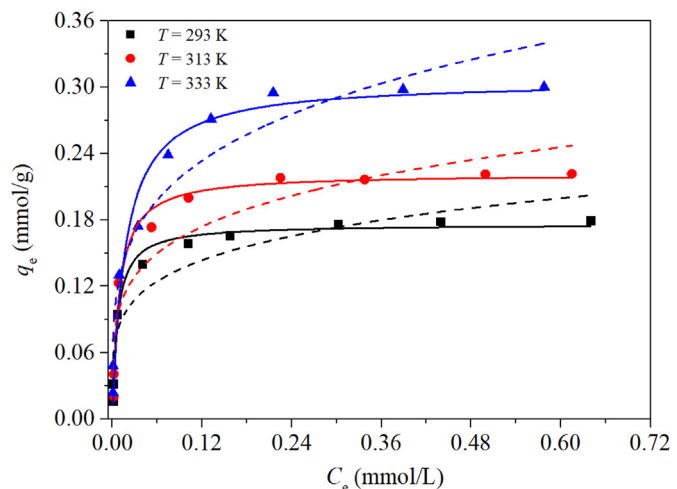


Fig. 3. Sorption isotherms and model fits of Ni(II) on cryptomelane. $\text{pH} = 7.0$, $m/V = 0.5\text{ g/L}$, $I = 0.01\text{ mol/L NaNO}_3$. Symbols represent the experimental sorption data, solid lines represent the fit curves of Langmuir model and dash lines represent the fit curves of Freundlich model.

type sorption isotherm curves suggest that the Ni(II) species are retained on cryptomelane surfaces by forming a monolayer coverage (Atasoy and Sahin, 2014; Mahmud et al., 2012). One can also rule out the possibility of Ni precipitation either on the cryptomelane surfaces or in the aqueous solution, both of which would result in the exponential growth of Ni(II) sorption amount. In addition, the positive correlation between sorption amount and solution temperature implies that the immobilization of Ni(II) by cryptomelane is an endothermal process. The sorption isotherms can be well fitted by the Langmuir model rather than the Freundlich model (see Fig. 3 and Table S2), pointing to a favorable chemisorption process of Ni(II) on cryptomelane (Bayramoglu et al., 2012; Yang et al., 2015).

3.3. Leaching data analysis

Table S3 lists the desorption percentages of Ni(II) from the metal-loaded samples prepared under different environmental conditions. At pH 4.0, more than 90% of the adsorbed Ni(II) is extracted by the $\text{CH}_3\text{COONH}_4$ ligand, suggesting that Ni(II) is predominately retained by cation exchange reaction and/or outer-sphere surface complexation with a small ratio of inner-sphere complexation. In contrast, the main sequestration mechanism changes to inner-sphere complexation at a higher pH value of 7.0. More specifically, the fraction of this binding mechanism increases from 85.9% to 95.3% as the temperature rises from 293 K to 333 K. This phenomenon implies that higher temperature facilitates the direct coordination of Ni(II) with the cryptomelane surface sites. At a highly alkaline pH value of 10.0, only 12.5% of the immobilized Ni(II) is desorbed by the EDTA-2Na ligand. Under such circumstances, the vast majority of Ni(II) (87.5%) is immobilized by forming insoluble solid phases.

3.4. Theoretical Ni(II) binding modes

The potential binding modes of Ni(II) by cryptomelane are predicted by considering their microstructures. Based on the previously reported crystallographic data (Vicat et al., 1986), the crystal structure of cryptomelane is illustrated by using Crystalmaker ver. 2.2.4 (Gong et al., 2014). As shown in Fig. 4, the framework of cryptomelane is constructed with edge-shared and corner-shared

MnO_6 octahedra, which results in the formation of one-dimensional (1×1) and two-dimensional (2×2) channels. The former is smaller and empty, whereas the latter is larger and contains some K^+ ions at the special position 2a ($0, 0, 0$) (Huang et al., 2010; Lu et al., 2007). The size of the larger channel ($\sim 4.6 \text{ \AA}$) is greater than the hydrated ionic radius (R_{H}) of $\text{Ni}(\text{II})$ (2.06 \AA) (Trivedi et al., 2001). In view of this, it is possible for the entrance of $\text{Ni}(\text{II})$ into these channels (Fig. 4A). Under the condition of exchanging with the K^+ ions, the central Ni would be surrounded by six equidistant hydrated O atoms at a $\text{Ni}-\text{O}$ interatomic distance ($R_{\text{Ni-O}}$) of $\sim 2.04 \text{ \AA}$, eight equidistant tunnel wall O atoms at $R_{\text{Ni-O}}$ of $\sim 2.85 \text{ \AA}$ and eight Mn atoms at $R_{\text{Ni-Mn}}$ of $\sim 3.56 \text{ \AA}$. In addition, $\text{Ni}(\text{II})$ can also attach on the cryptomelane surfaces due to electrostatic interaction, forming outer-sphere surface complexes (Fig. 4B). Moreover, the NiO_6 octahedra can directly coordinate with the Mn–O sites via single corner-shared (SCS, Fig. 4C), double corner-shared (DCS, Fig. 4D), triple corner-shared (TCS, Fig. 4E) and edge-shared (ES, Fig. 4F) modes, forming multiple inner-sphere surface complexes. The specific coordination geometry of $\text{Ni}(\text{II})$ can be calculated by integrating the EXAFS-derived $R_{\text{Ni-O}}$ value of $\sim 2.04 \text{ \AA}$ and the structural parameters of cryptomelane (see the detailed calculation strategies in SI) (Gao et al., 2008; Sheng et al., 2011a, b; Tan et al., 2017; Vicat et al., 1986). Specifically, the theoretical $R_{\text{Ni-Mn}}$ values would be $3.88\text{--}4.02 \text{ \AA}$, $3.52\text{--}3.64 \text{ \AA}$ and $2.74\text{--}2.84 \text{ \AA}$ for the SCS, DCS/TCS and ES linkage modes, respectively. In case of lattice substitution (i.e., incorporation of $\text{Ni}(\text{II})$ at the Mn vacancies (INC) of cryptomelane, Fig. 4G), the central Ni atom is expected to be surrounded by six Mn atoms at $R_{\text{Ni-Mn}}$ of $2.87\text{--}2.93 \text{ \AA}$ (Cloud, 1958).

3.5. Spectroscopic identification on the immobilization mechanisms

3.5.1. FTIR analysis

Fig. S3 shows the FTIR spectra of pristine and $\text{Ni}(\text{II})$ -bound cryptomelane samples formed at pH 7.0 and three different

temperatures. After the binding of $\text{Ni}(\text{II})$, the characteristic Mn–O absorption peaks at 460 and 510 cm^{-1} become wider and shift to higher wavenumbers (insert in Fig. S3). One can conclude that the Mn–O bonds are involved in capturing $\text{Ni}(\text{II})$ at a neutral pH of 7.0 (Dinh et al., 2018). In other words, $\text{Ni}(\text{II})$ is retained via inner-sphere complexation with the Mn–O sites.

3.5.2. XPS analysis

The XPS spectra of cryptomelane samples before and after $\text{Ni}(\text{II})$ retention at pH 7.0 are illustrated in Fig. 5. The wide scan spectrum of pristine cryptomelane exhibits the C 1s, O 1s, Mn 2p and Mn 3s peaks (see the dash lines in Fig. 5A). In addition, the interaction of $\text{Ni}(\text{II})$ with cryptomelane results in the appearance of Ni 2p peak (see the dot line in Fig. 5A). Herein, we carefully analyze the narrow scans of the O 1s, Mn 2p and Mn 3s peaks. Specifically, the binding energy of O 1s peak shifts to a higher value after the immobilization of $\text{Ni}(\text{II})$ (Fig. 5B), revealing the coordination of $\text{Ni}(\text{II})$ with the O-containing sites located on the cryptomelane surfaces (Chen et al., 2016; Pan et al., 2012).

The Mn 2p spectrum (Fig. 5C) exhibits two peaks, i.e., $\text{Mn } 2p_{1/2}$ at the binding energy of 654.0 eV and $\text{Mn } 2p_{3/2}$ at the binding energy of 642.2 eV . Herein, the energy separation of 11.8 eV is well consistent with that of MnO_2 (Tang et al., 2007). Cryptomelane possesses multiple Mn oxidation states in its crystal structure. However, it is impossible to distinguish Mn^{2+} , Mn^{3+} and Mn^{4+} ions from the Mn 2p spectrum due to their similar binding energies (Fan et al., 2008; Tang et al., 2007). In view of this, the Mn 3s spectra are analyzed to further identify the specific Mn oxidation states (Fan et al., 2008; Galakhov et al., 2002; Ilton et al., 2016; Khatiwada et al., 2018; Tang et al., 2007). As shown in Fig. 5D, the 3s splitting between the main and satellite peaks is $\sim 4.8 \text{ eV}$ for all the samples. According to the relationship between different Mn valence states and their corresponding Mn 3s energy gaps (see Fig. S4 and the detailed information in SI) (Galakhov et al., 2002),

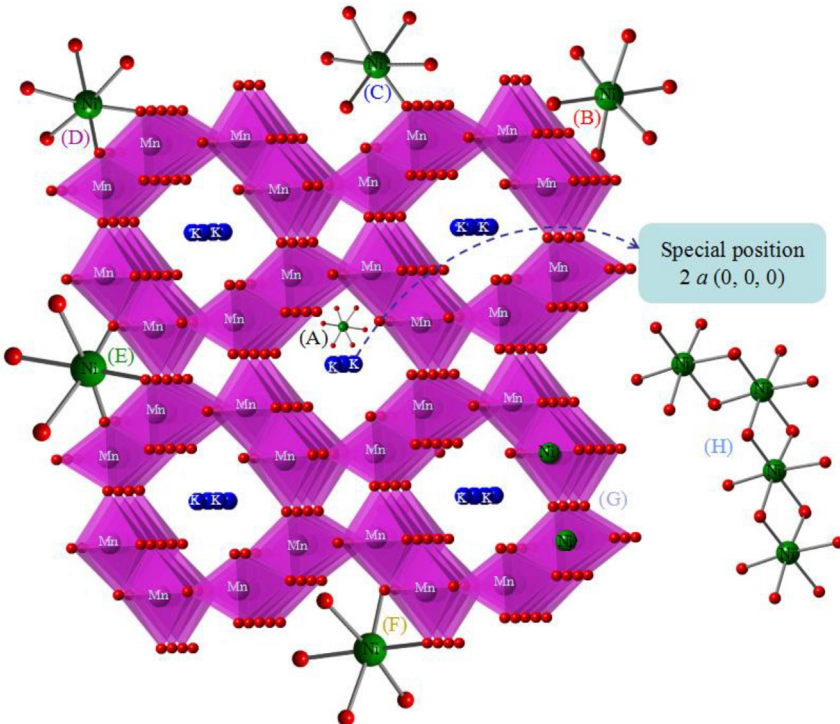


Fig. 4. Potential immobilization mechanisms of $\text{Ni}(\text{II})$ by the cryptomelane mineral. A: cation exchange; B: outer-sphere surface complexation; C: SCS inner-sphere surface complexation; D: DCS inner-sphere surface complexation; E: TCS inner-sphere surface complexation; F: ES inner-sphere surface complexation; G: incorporation of $\text{Ni}(\text{II})$ at the Mn vacancies (INC); H: Precipitation of $\text{Ni}(\text{OH})_2$ phase.

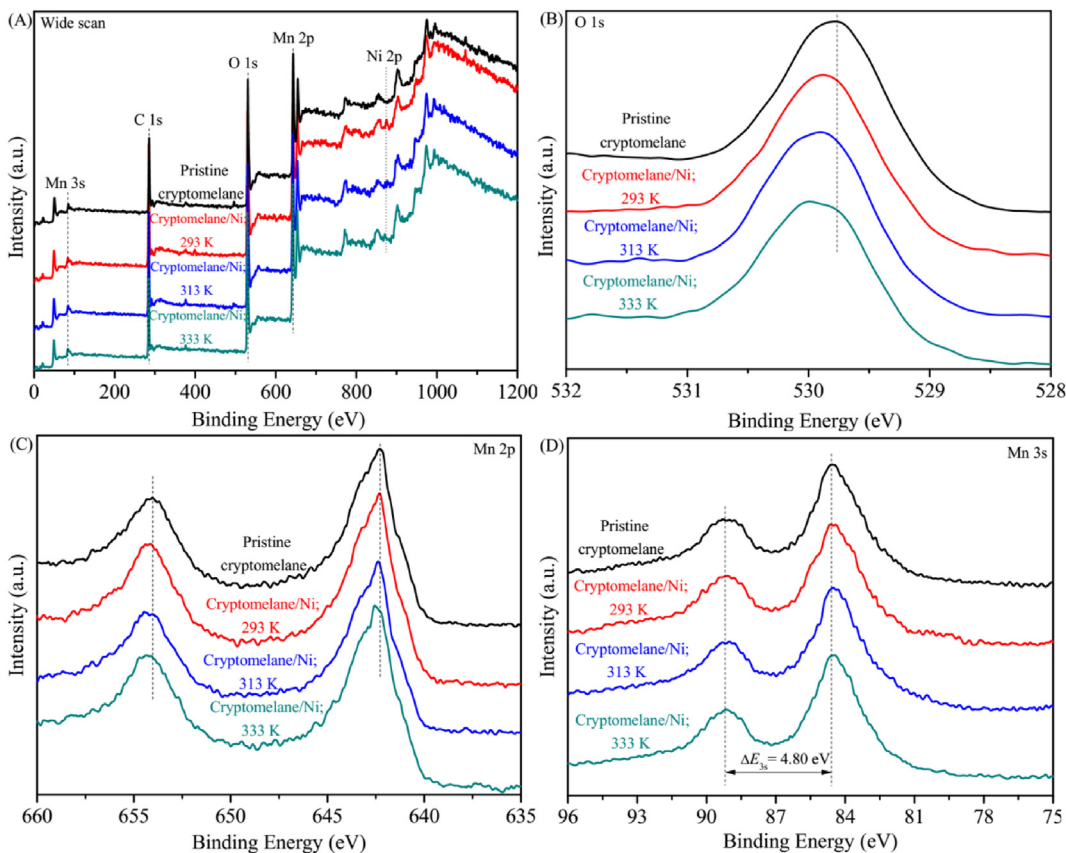


Fig. 5. XPS survey scans (A), high-resolution O 1s (B), Mn 2p (C) and Mn 3s (D) spectra of cryptomelane samples before and after Ni(II) sorption at different temperatures. pH = 7.0, m/V = 0.5 g/L, $C_{\text{Ni(II)}}^{\text{initial}} = 1.0 \times 10^{-4} \text{ mol/L}$, I = 0.01 mol/L NaNO₃.

the average oxidation state (AOS) of Mn is calculated to be ~3.70. This result suggests the simultaneous presence of Mn⁴⁺ and Mn³⁺ ions in the cryptomelane structure with Mn⁴⁺ as the principal component. It is also worth noting that the rising of temperature and the increased sorption of Ni(II) have no effect on the structure of cryptomelane. In view of this, one can preliminarily excludes the possibility of Ni²⁺ ions substitution for Mn³⁺/Mn⁴⁺ ions in the lattice structure, under which condition the AOS of Mn would change due to the variation of molar Mn³⁺:Mn⁴⁺ ratio. Hence, the immobilization of Ni(II) by the cryptomelane mineral at pH 7.0 can be ascribed as inner-sphere complexation.

3.5.3. EXAFS analysis

The specific microstructures of Ni(II) on cryptomelane under different environmental conditions can be determined from the analyses of EXAFS spectra. As illustrated in Fig. 6A, the $k^3\chi(k)$ spectrum of the cryptomelane/Ni sample prepared at pH 4.0 is quite similar to that of Ni(II)(aq), suggesting Ni(II) is retained in its hydrated state. By contrast, the spectra of the cryptomelane/Ni samples prepared at pH 7.0 are clearly disparate from those of Ni(II)(aq) and α -Ni(OH)₂(s). This phenomenon reveals that the predominant sequestration mechanism of Ni(II) by cryptomelane is neither cation exchange/outer-sphere complexation nor precipitation. Alternatively, the appearance of a bulge at ~5.3 Å⁻¹ (marked by ellipse) and two pits at ~7.8 and 9.7 Å⁻¹ (marked by rectangles) points to the generation of Ni(II) inner-sphere complexes on cryptomelane surfaces (Dähn et al., 2002; Ren et al., 2013; Sheng et al., 2011a, b; Yang et al., 2015). More specifically, the oscillation intensities of these spectral features gradually increase with rising temperature, suggesting the presence of stronger backscattering

signals from the surrounding atoms under higher temperature condition. The spectrum of the cryptomelane/Ni sample collected at pH 10.0 is basically analogous to that of α -Ni(OH)₂(s), implying the occurrence of hydroxide precipitation under high alkaline condition. Note that the k^3 -weighted spectra of all the cryptomelane/Ni samples are obviously different from that of the Ni cop Mn sample (i.e., Ni(II) co-precipitation with cryptomelane, see the detailed information in SI). Hence, the immobilization of Ni(II) under our experimental conditions is not predominantly by the incorporation (lattice substitution) mechanism.

For all the samples, the Fourier transformed radial structural functions (RSFs) show a narrow and strong peak at ~1.60 Å (phase shift uncorrected) (marked by the dash line in Fig. 6B). The similarities in the intensity and position of this peak for different samples indicate that the change of environmental conditions has negligible influence on the coordination of central Ni atoms with the surrounding O atoms. For the cryptomelane/Ni samples prepared at pH 7.0, the RSFs exhibit additional peaks centered at ~2.35 Å (marked by ellipse) and ~3.00 Å (marked by rectangle) (phase shift uncorrected), pointing to the contribution of higher backscattering paths such as Ni–Mn and/or Ni–Ni. In addition, the peak intensity at ~2.35 Å (phase shift uncorrected) keeps almost unchanged with the increase of solution temperature, while that at ~3.00 Å (phase shift uncorrected) gradually increases with rising temperature. However, in a previous study involving the sorption of Ni(II) on δ -MnO₂, Manceau et al. (2007) found that the peak intensity at ~3.10 Å (phase shift uncorrected) gradually decreased with the increase of Ni(II) sorption amount. The difference herein suggests that Ni(II) exhibits disparate binding modes on various manganese oxide surfaces due to the different mineral features

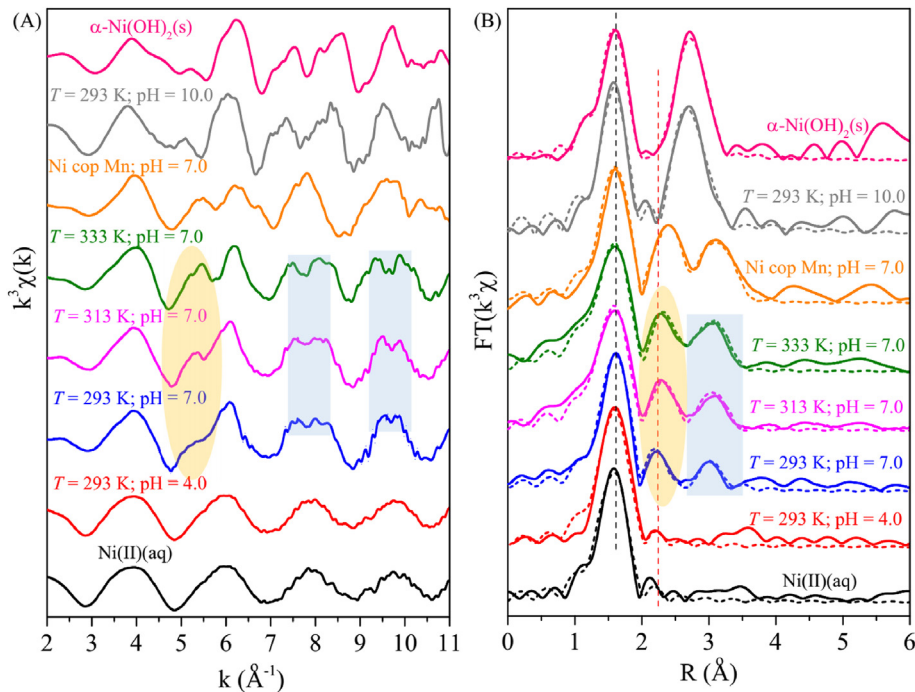


Fig. 6. k^3 -weighted EXAFS spectra (A) and corresponding RSFs (phase shift uncorrected) (B) of Ni-containing reference and uptake samples. Solid lines represent the experimental spectra and dash lines represent the least-square fit curves.

(e.g., morphology, crystalline structure and surface properties) and different experimental conditions (e.g., aging time, temperature, pH and dissolved Ni(II) concentration).

Table S4 lists the structural parameters obtained from the least-square fits of the RSFs. For the sample collected at pH 4.0, the central Ni atom is coordinated by ~6.0 O atoms at $R_{\text{Ni}-\text{O}}$ of ~2.04 Å, being analogous to those of Ni(II)(aq). In view of this, the hydrated $\text{Ni}(\text{H}_2\text{O})_6^{2+}$ ions are possibly retained in cryptomelane channels via ion exchange (with the K^+ ions at the special position 2 a (0, 0, 0) or the H^+ ions, Fig. 4A) or attached on cryptomelane surfaces via electrostatic interaction (Fig. 4B). In the case of Ni(II) exchanging with K^+ ions, the foregoing theoretical simulation predicts the presence of additional Ni–O path at ~2.85 Å and Ni–Mn path at ~3.56 Å in addition to the Ni–O shell at ~2.04 Å. Herein, the absence of these structural parameters suggests that Ni(II) may replace the H^+ ions rather than the K^+ ions in the channels at an acidic pH value of 4.0. The RSFs of the samples prepared at pH 7.0 include two Ni–Mn paths at $R_{\text{Ni}-\text{Mn}1}$ of ~2.85 Å and $R_{\text{Ni}-\text{Mn}2}$ of ~3.48 Å. According to the above theoretical simulation (Fig. 4C–G) and the previous studies (Grangeon et al., 2017; Lefkowitz and Elzinga, 2017; Manceau et al., 2007; Peacock and Sherman, 2007; Peacock, 2009; Peña et al., 2010; Simanova et al., 2015; Singh et al., 2002; Yin et al., 2014), the shorter Ni–Mn path at ~2.85 Å possibly arises from the ES binding between NiO_6 and MnO_6 octahedra or the incorporation of Ni(II) at the vacancies (INC). In contrast, the longer Ni–Mn path at ~3.48 Å may be attributed to the DCS or TCS configurations between NiO_6 and MnO_6 octahedra. More specifically, the binding modes with similar $R_{\text{Ni}-\text{Mn}}$ values can be further distinguished from the differences of their corresponding coordination numbers ($\text{CN}_{\text{Ni}-\text{Mn}}$), i.e., 1.0–2.0 for ES vs. 6.0 for INC, and 2.0 for DCS vs. 6.0 for TCS. In the present study, with the solution temperature rising from 293 K to 333 K, the $\text{CN}_{\text{Ni}-\text{Mn}}$ value at ~2.85 Å keeps at a constant value of ~1.5, while that at ~3.48 Å increases from ~1.6 to ~2.4 (Table S4). Clearly, Ni(II) forms both ES and DCS binding modes with the cryptomelane edge sites. More specifically, the relative ratio of ES mode keeps constant with increasing temperature, while that of

DCS configuration increases with rising temperature. In general, the ES configuration (corresponding to a shorter but stronger Ni–Mn bond) is more stable than the DCS linkage (corresponding to a longer but weaker Ni–Mn bond) (Elzinga and Reeder, 2002; Yang et al., 2013). Thereby, the enhancement of Ni(II) sorption amount with rising temperature (Fig. 3) is caused by the increase of weak DCS configuration. The absence of TCS linkage mode is reasonable in consideration of the cryptomelane properties. It was reported that the binding modes of Ni(II) with manganese minerals were greatly dependent on the AOS of Mn, i.e., the predominant binding mode transferred from TCS to DCS as the AOS value decreased from 3.95 to 3.65 (Grangeon et al., 2017; Simanova et al., 2015). Herein, the Mn AOS value of 3.70 for our cryptomelane sample (see section 5.2 and Fig. S4 in SI) would facilitate the occurrence of inner-sphere surface complexation in DCS mode. The structural parameters for the sample prepared at a highly alkaline pH value of 10.0 ($R_{\text{Ni}-\text{Ni}} \sim 3.07$ Å and $\text{CN}_{\text{Ni}-\text{Ni}} \sim 3.6$ as listed in Table S4) indicate the generation of $\alpha\text{-Ni(OH)}_2\text{(s)}$ phase rather than the most stable $\beta\text{-Ni(OH)}_2\text{(s)}$ solid with a larger $R_{\text{Ni}-\text{Ni}}$ value of 3.12–3.13 Å (Dähn et al., 2002; Ren et al., 2013; Yang et al., 2011, 2012). The formation of nickel hydroxide precipitate predicted from the EXAFS analysis is consistent with the speciation calculation (Fig. S2) and ligand extraction data (Table S3 and section 3.3).

4. Conclusions

The synergistic application of multiple analysis approaches facilitate the quantitative and molecular-scale understanding on the interaction mechanisms between Ni(II) and cryptomelane. As the aqueous pH rises from 4.0 to 7.0 and finally 10.0, the immobilization mechanism of Ni(II) by cryptomelane transfers from cation exchange (migration into the 2×2 channels)/outer-sphere complexation (attachment on the surfaces) to inner-sphere complexation (in both the ES and DCS linkage modes) and finally precipitation. The rising of temperature enhances the sorption capacity of cryptomelane towards Ni(II) due to the increased

proportion of DCS surface binding mode. The formed Ni(II) species with different thermodynamic stabilities would further affect their migration trend and fate. Given the complexity of the geological environment and the widespread distribution of various manganese minerals in the aquatic systems, additional studies are required to further explore the reversibility of the retained Ni(II) species upon the fluctuations of environment conditions (e.g., the decrease of aqueous pH, the extension of aging time and the discharge of new pollutants) and the triggered transformation of manganese oxide phases.

Acknowledgements

C. Wu and L. Chen contributed equally to this paper. Financial supports from the National Natural Science Foundation of China (21790370, U1732132, 41773004), "Young Thousand Talented Program" in China and the Priority Academic Program Development (PAPD) of Jiangsu Higher Education Institutions are acknowledged.

Appendix A. Supplementary data

Supplementary data related to this article can be found at <https://doi.org/10.1016/j.chemosphere.2018.07.029>.

References

- Ankudinov, A.L., Rehr, J.J., 1997. Relativistic calculations of spin-dependent X-ray-absorption spectra. *Phys. Rev. B* 56, 1712–1715.
- Atasoy, A.D., Sahin, M.O., 2014. Adsorption of fluoride on the raw and modified cement clay. *Clean - Soil, Air, Water* 42, 415–420.
- Bayramoglu, G., Arica, M.Y., Adiguzel, N., 2012. Removal of Ni(II) and Cu(II) ions using native and acid treated Ni-hyperaccumulator plant *Alyssum discolor* from Turkish serpentine soil. *Chemosphere* 89, 302–309.
- Bui, T.X., Choi, H., 2010. Influence of ionic strength, anions, cations, and natural organic matter on the adsorption of pharmaceuticals to silica. *Chemosphere* 80, 681–686.
- Calvert, C., Joesten, R., Ngala, K., Villegas, J., Morey, A., Shen, X.F., Suib, S.L., 2008. Synthesis, characterization, and rietveld refinement of tungsten-framework-doped porous manganese oxide (K-OMS-2) material. *Chem. Mater.* 20, 6382–6388.
- Cempel, M., Nikel, G., 2006. Nickel: a review of its sources and environmental toxicology. *Pol. J. Environ. Stud.* 15, 375–382.
- Chen, L.L., Zhao, D.L., Chen, S.H., Wang, X.B., Chen, C.L., 2016. One-step fabrication of amino functionalized magnetic graphene oxide composite for uranium(VI) removal. *J. Colloid Interface Sci.* 472, 99–107.
- Chen, X., Shen, Y.F., Suib, S.L., O'Young, C.L., 2002. Characterization of manganese oxide octahedral molecular sieve (M-OMS-2) materials with different metal cation dopants. *Chem. Mater.* 14, 940–948.
- Cloud, W.H., 1958. Crystal structure and ferrimagnetism in NiMnO_3 and CoMnO_3 . *Phys. Rev.* 111, 1046–1049.
- Dähn, R., Scheidegger, A.M., Manceau, A., Schlegel, M.L., Baeyens, B., Bradbury, M.H., Morales, M., 2002. Neformation of Ni phyllosilicate upon Ni uptake on montmorillonite: a kinetics study by powder and polarized extended X-ray absorption fine structure spectroscopy. *Geochim. Cosmochim. Acta* 66, 2335–2347.
- DeGuzman, R.N., Shen, Y.F., Neth, E.J., Suib, S.L., O'young, C.L., Levine, S., Newsam, J.M., 1994. Synthesis and characterization of octahedral molecular sieves (OMS-2) having the hollardite structure. *Chem. Mater.* 6, 815–821.
- Dinh, V.P., Le, N.C., Tuyen, L.A., Hung, N.Q., Nguyen, V.D., Nguyen, N.T., 2018. Insight into adsorption mechanism of lead(II) from aqueous solution by chitosan loaded MnO_2 nanoparticles. *Mater. Chem. Phys.* 207, 294–302.
- El-Naggar, I.M., El-Absy, M.A., Abdel-Hamid, M.M., Aly, H.F., 1993. Sorption behaviour of uranium and thorium on cryptomelane-type hydrous manganese dioxide from aqueous solution. *Solvent Extr. Ion Exch.* 11, 521–540.
- Elzinga, E.J., Reeder, R.J., 2002. X-ray absorption spectroscopy study of Cu^{2+} and Zn^{2+} adsorption complexes at the calcite surface: implications for site-specific metal incorporation preferences during calcite crystal growth. *Geochem. Cosmochim. Acta* 66, 3943–3954.
- Fan, C.Z., Lu, A.H., Li, Y., Wang, C.Q., 2008. Synthesis, characterization, and catalytic activity of cryptomelane nanomaterials produced with industrial manganese sulfate. *J. Colloid Interface Sci.* 327, 393–402.
- Galakhov, V.R., Demeter, M., Bartkowski, S., Neumann, M., Ovechkina, N.A., Kurmaev, E.Z., Logachevskaya, N.I., Mukovskii, Y.M., Mitchell, J., Ederer, D.L., 2002. Mn 3s exchange splitting in mixed-valence manganites. *Phys. Rev. B* 65, 113102.
- Gao, T., Glerup, M., Krumeich, F., Nesper, R., Fjellvåg, H., Norby, P., 2008. Microstructures and spectroscopic properties of cryptomelane-type manganese dioxide nanofibers. *J. Phys. Chem. C* 112, 13134–13140.
- Gao, Y., Kan, A.T., Tomson, M.B., 2003. Critical evaluation of desorption phenomena of heavy metals from natural sediments. *Environ. Sci. Technol.* 37, 5566–5573.
- Ghaly, M., El-Sherief, E.A., Metwally, S.S., Saad, E.A., 2018. Utilization of nanocryptomelane for the removal of cobalt, cesium and lead ions from multi-component system: kinetic and equilibrium studies. *J. Hazard Mater.* 352, 1–16.
- Ghoneimy, H.F., 1997. Adsorption of Co^{2+} and Zn^{2+} on cryptomelane-type hydrous manganese dioxide. *J. Radioanal. Nucl. Chem.* 223, 61–65.
- Gong, Y.X., Yatongchai, C., Wren, A.W., Mellott, N.P., 2014. Reintroducing sborgite: crystallization through exposure of sodium borosilicate glasses to moisture. *Mater. Lett.* 136, 265–270.
- Grangeon, S., Fernandez-Martinez, A., Claret, F., Marty, N., Tournassat, C., Warmor, F., Glotere, A., 2017. In-situ determination of the kinetics and mechanisms of nickel adsorption by nanocrystalline vernadite. *Chem. Geol.* 459, 24–31.
- Gustafsson, J.P., 2018. Visual MINTEQ, version 3.1; Department of Land and Water Resources Engineering, KTH (Royal Institute of Technology): Stockholm. Available for free download at the website of <http://vminteq.lvr.kth.se/download/>.
- Ho, Y.S., McKay, G., 1999a. Pseudo-second order model for sorption processes. *Process Biochem.* 34, 451–465.
- Ho, Y.S., McKay, G., 1999b. A kinetic study of dye sorption by biosorbent waste product pith. *Resour. Conserv. Recycl.* 25, 171–193.
- Ho, Y.S., Ofomaja, A.E., 2006. Pseudo-second-order model for lead ion sorption from aqueous solutions onto palm kernel fiber. *J. Hazard Mater.* 129, 137–142.
- Hu, B.W., Cheng, W., Zhang, H., Yang, S.T., 2010. Solution chemistry effects on sorption behavior of radionuclide $^{63}\text{Ni}(\text{II})$ in illite-water suspensions. *J. Nucl. Mater.* 406, 263–270.
- Huang, H., Sithambaran, S., Chen, C.H., Kithongo, C.K., Xu, L.P., Iyer, A., Garces, H.F., Suib, S.L., 2010. Microwave-assisted hydrothermal synthesis of cryptomelane-type octahedral molecular sieves (OMS-2) and their catalytic studies. *Chem. Mater.* 22, 3664–3669.
- Ilton, E.S., Post, J.E., Heaney, P.J., Ling, F.T., Kerisit, S.N., 2016. XPS determination of Mn oxidation states in Mn (hydr)oxides. *Appl. Surf. Sci.* 366, 475–485.
- Ivanets, A.I., Srivastava, V., Kitikova, N.V., Shashkov, I.L., Sillanpää, M., 2017. Kinetic and thermodynamic studies of the Co(II) and Ni(II) ions removal from aqueous solutions by Ca-Mg phosphates. *Chemosphere* 171, 348–354.
- Julien, C.M., Massot, M., Poinsignon, C., 2004. Lattice vibrations of manganese oxides Part I. Periodic structures. *Spectrochim. Acta* 60, 689–700.
- Kazazi, M., 2018. Effect of electrodeposition current density on the morphological and pseudocapacitance characteristics of porous nano-spherical MnO_2 electrode. *Ceram. Int.* 44, 10863–10870.
- Khatiwada, R., Olivares, C., Abrell, L., Root, R.A., Sierra-Alvarez, R., Field, J.A., Chorover, J., 2018. Oxidation of reduced daughter products from 2,4-dinitroanisole (DNAN) by Mn(IV) and Fe(III) oxides. *Chemosphere* 201, 790–798.
- Lefkowitz, J.P., Elzinga, E.J., 2017. Structural alteration of hexagonal birnessite by aqueous Mn(II): impacts on Ni(II) sorption. *Chem. Geol.* 466, 524–532.
- Li, H., Liu, F., Zhu, M.Q., Feng, X.H., Zhang, J., Yin, H., 2015. Structure and properties of Co-doped cryptomelane and its enhanced removal of Pb^{2+} and Cr^{3+} from wastewater. *J. Environ. Sci.* 34, 77–85.
- Lu, A.H., Gao, X., Wang, C.Q., Gao, Y.W., Zheng, D.S., Chen, T.H., Zhao, D.J., Qin, S., 2007. Natural cryptomelane and its potential application in the adsorption of heavy metal cadmium. *J. Mineral. Petrol. Sci.* 102, 217–225.
- Mahmud, K., Islam, M.A., Mitsionis, A., Albanis, T., Vaimakis, T., 2012. Adsorption of direct yellow 27 from water by poorly crystalline hydroxyapatite prepared via precipitation method. *Desalin. Water Treat.* 41, 170–178.
- Manceau, A., Kersten, M., Marcus, M.A., Geoffroy, N., Granina, L., 2007. Ba and Ni speciation in a nodule of binary Mn oxide phase composition from Lake Baikal. *Geochim. Cosmochim. Acta* 71, 1967–1981.
- Mercer, K.L., Tobias, J.E., 2008. Removal of arsenic from high ionic strength solutions: effects of ionic strength, pH, and preformed versus in situ formed HFO. *Environ. Sci. Technol.* 42, 3797–3802.
- Pan, S.D., Zhang, Y., Shen, H.Y., Hu, M.Q., 2012. An intensive study on the magnetic effect of mercapto-functionalized nano-magnetic Fe_3O_4 polymers and their adsorption mechanism for the removal of Hg(II) from aqueous solution. *Chem. Eng. J.* 210, 564–574.
- Peacock, C.L., 2009. Physiochemical controls on the crystal-chemistry of Ni in birnessite: genetic implications for ferromanganese precipitates. *Geochem. Cosmochim. Acta* 73, 3568–3578.
- Peacock, C.L., Sherman, D.M., 2007. Sorption of Ni by birnessite: equilibrium controls on Ni in seawater. *Chem. Geol.* 238, 94–106.
- Peña, J., Kwon, K.D., Refson, K., Bargar, J.R., Sposito, G., 2010. Mechanisms of nickel sorption by a bacteriogenic birnessite. *Geochem. Cosmochim. Acta* 74, 3076–3089.
- Randall, S.R., Sherman, D.M., Ragnarsdottir, K.V., 1998. An extended X-ray absorption fine structure spectroscopy investigation of cadmium sorption on cryptomelane ($\text{KMn}_2\text{O}_{10}$). *Chem. Geol.* 151, 95–106.
- Ravel, B., Newville, M., 2005. ATHENA, ARTEMIS, HEPHAESTUS: data analysis for X-ray absorption spectroscopy using IFEFFIT. *J. Synchrotron Radiat.* 12, 537–541.
- Ren, X.M., Yang, S.T., Hu, F.C., He, B., Xu, J.Z., Tan, X.L., Wang, X.K., 2013. Microscopic level investigation of Ni(II) sorption on Na-rectorite by EXAFS technique combined with statistical F-tests. *J. Hazard Mater.* 252–253, 2–10.
- Salinas, E., de Orellano, M.E., Rezza, I., Martinez, L., Marchesky, E., de Tosetti, M.S., 2000. Removal of cadmium and lead from dilute aqueous solutions by *Rhodotorula rubra*. *Bioresour. Technol.* 72, 107–112.
- Scheckel, K.G., Sparks, D.L., 2000. Kinetics of the formation and dissolution of Ni

- precipitates in a gibbsite/amorphous silica mixture. *J. Colloid Interface Sci.* 229, 222–229.
- Sheng, G., Hu, J., Jin, H., Yang, S., Ren, X., Li, J., Chen, Y., Wang, X., 2010. Effect of humic acid, fulvic acid, pH, ionic strength and temperature on $^{63}\text{Ni}(\text{II})$ sorption to MnO_2 . *Radiochim. Acta* 98, 291–299.
- Sheng, G.D., Sheng, J., Yang, S.T., Hu, J., Wang, X.K., 2011a. Behavior and mechanism of Ni(II) uptake on MnO_2 by a combination of macroscopic and EXAFS investigation. *J. Radioanal. Nucl. Chem.* 289, 129–135.
- Sheng, G.D., Yang, S.T., Sheng, J., Hu, J., Tan, X.L., Wang, X.K., 2011b. Macroscopic and microscopic investigation of Ni(II) sequestration on diatomite by Batch, XPS, and EXAFS techniques. *Environ. Sci. Technol.* 45, 7718–7726.
- Siebecker, M., Li, W., Khalid, S., Sparks, D., 2014. Real-time QEXAFS spectroscopy measures rapid precipitate formation at the mineral-water interface. *Nat. Commun.* 5, 5003.
- Simanova, A.A., Kwon, K.D., Bone, S.E., Bargar, J.R., Refson, K., Sposito, G., Peña, J., 2015. Probing the sorption reactivity of the edge surfaces in birnessite nanoparticles using nickel(II). *Geochem. Cosmochim. Acta* 164, 191–204.
- Singh, B., Sherman, D.M., Gilkes, R.J., Wells, M.A., Mosselmans, J.F.W., 2002. Incorporation of Cr, Mn and Ni into goethite ($\alpha\text{-FeOOH}$): mechanism from extended X-ray absorption fine structure spectroscopy. *Clay Miner.* 37, 639–649.
- Sithambaram, S., Xu, L.P., Chen, C.H., Ding, Y.S., Kumar, R., Calvert, C., Suib, S.L., 2009. Manganese octahedral molecular sieve catalysts for selective styrene oxide ring opening. *Catal. Today* 140, 162–168.
- Tan, X.L., Fang, M., Ren, X.M., Mei, H.Y., Shao, D.D., Wang, X.K., 2014. Effect of silicate on the formation and stability of Ni-Al LDH at the $\gamma\text{-Al}_2\text{O}_3$ surface. *Environ. Sci. Technol.* 49, 6363–6363.
- Tan, X.L., Liu, G., Mei, H.Y., Fang, M., Ren, X.M., Chen, C.L., 2017. The influence of dissolved Si on Ni precipitate formation at the kaolinite water interface: kinetics, DRS and EXAFS analysis. *Chemosphere* 173, 135–142.
- Tang, X.F., Li, Y.G., Chen, J.L., Xu, Y.D., Shen, W.J., 2007. Synthesis, characterization, and catalytic application of titanium-cryptomelane nanorods/fibers. *Microporous Mesoporous Mater.* 103, 250–256.
- Tizfahm, J., Aghazadeh, M., Maragheh, M.G., Ganjali, M.R., Norouzi, P., Faridbod, F., 2016. Electrochemical preparation and evaluation of the supercapacitive performance of MnO_2 nanoworms. *Mater. Lett.* 167, 153–156.
- Trivedi, P., Axe, L., Tyson, T.A., 2001. XAS studies of Ni and Zn sorbed to hydrous manganese oxide. *Environ. Sci. Technol.* 35, 4515–4521.
- Vicat, J., Fanchon, E., Strobel, P., Qui, D.T., 1986. The structure of $\text{K}_{1.33}\text{Mn}_8\text{O}_{16}$ and cation ordering in hollandite-type structures. *Acta Crystallogr. B* 42, 162–167.
- Villegas, J.C., Garces, L.J., Gomez, S., Durand, J.P., Suib, S.L., 2005. Particle size control of cryptomelane nanomaterials by use of H_2O_2 in acidic conditions. *Chem. Mater.* 17, 1910–1918.
- Wang, X., Li, Y.D., 2002. Selected-control hydrothermal synthesis of alpha- and beta- MnO_2 single crystal nanowires. *J. Am. Chem. Soc.* 124, 2880–2881.
- Wang, Z., Meador, J.P., Leung, K.M.Y., 2016. Metal toxicity to freshwater organisms as a function of pH: a meta-analysis. *Chemosphere* 144, 1544–1552.
- Xu, L., Zheng, T., Yang, S.T., Zhang, L.J., Wang, J.Q., Liu, W., Chen, L.H., Diwu, J., Chai, Z.F., Wang, S.A., 2016. Uptake mechanisms of Eu(III) on hydroxyapatite: a potential permeable reactive barrier backfill material for trapping trivalent minor actinides. *Environ. Sci. Technol.* 50, 3852–3859.
- Xu, Y., Axe, L., Boonfueng, T., Tyson, T.A., Trivedi, P., Pandya, K., 2007. Ni(II) complexation to amorphous hydrous ferric oxide: an X-ray absorption spectroscopy study. *J. Colloid Interface Sci.* 314, 10–17.
- Yang, S.T., Ren, X.M., Zhao, G.X., Shi, W.Q., Montavon, G., Grambow, B., Wang, X.K., 2015. Competitive sorption and selective sequence of Cu(II) and Ni(II) on montmorillonite: batch, modeling, EPR and XAS studies. *Geochem. Cosmochim. Acta* 166, 129–145.
- Yang, S.T., Sheng, G.D., Guo, Z.Q., Tan, X.L., Xu, J.Z., Wang, X.K., 2012. Investigation of radionuclide $^{63}\text{Ni}(\text{II})$ sequestration mechanisms on mordenite by batch and EXAFS spectroscopy study. *Sci. China Chem.* 55, 632–642.
- Yang, S.T., Sheng, G.D., Montavon, G., Guo, Z.Q., Tan, X.L., Grambow, B., Wang, X.K., 2013. Investigation of Eu(III) immobilization on $\gamma\text{-Al}_2\text{O}_3$ surfaces by combining batch technique and EXAFS analyses: role of contact time and humic acid. *Geochem. Cosmochim. Acta* 121, 84–104.
- Yang, S.T., Sheng, G.D., Tan, X.L., Hu, J., Du, J.Z., Montavon, G., Wang, X.K., 2011. Determination of Ni(II) uptake mechanisms on mordenite surfaces: a combined macroscopic and microscopic approach. *Geochem. Cosmochim. Acta* 75, 6520–6534.
- Yin, H., Li, H., Wang, Y., Ginder-Vogel, M., Qiu, G.H., Feng, X.H., Zheng, L.R., Liu, F., 2014. Effects of Co and Ni co-doping on the structure and reactivity of hexagonal birnessite. *Chem. Geol.* 381, 10–20.
- Yuan, F., Wu, C.F., Cai, Y.W., Zhang, L.J., Wang, J.Q., Chen, L.H., Wang, X.K., Yang, S.T., Wang, S.A., 2017. Synthesis of phytic acid-decorated titanate nanotubes for high efficient and high selective removal of U(VI). *Chem. Eng. J.* 322, 353–365.
- Zhao, X.L., Qiang, S.R., Wu, H.Y., Yang, R.B., Shao, D.D., Fang, L.C., Liang, J.J., Li, P., Fan, Q.H., 2017. Exploring the sorption mechanism of Ni(II) on illite: batch Sorption, Modelling, EXAFS and extraction investigations. *Sci. Rep.* 7, 8495.